ROYAL SOCIETY OF CHEMISTRY

PAPER

Check for updates

UVC-induced valence switching in BaFBr:Sm^{3+} nanoplates

Nishani T. Manamperi and Federico A. Rabuffetti [ID] *

UVC-induced valence switching in nanocrystalline BaFBr:Sm^{3+} was studied in the context of photoexcitable storage phosphors. Nanocrystals were synthesized *via* hot-injection thermolysis of metal bromodifluoroacetates and consisted of square plates with average dimensions 34.4 nm (edge) × 4.9 nm (thickness); polydispersities in both dimensions were less than 10%. Nanoplates were found to undergo partial reduction upon exposure to UVC radiation of wavelength equal to 185 nm to yield BaFBr codoped with Sm^{3+} and Sm^{2+}. Luminescence studies were conducted to probe a number of aspects of this photochemical reaction, including extent, kinetics, reversibility, and stability of photogenerated Sm^{2+} ions. Photoreduction extent depended on atmosphere (air *vs.* vacuum) and sample treatment (as-prepared *vs.* preheated), revealing the presence of photoactive centers at or near the surface of the nanoplates. Photoreduction kinetics was rationalized invoking a bimodal distribution of photoactive centers in which electron-trapping Sm^{3+} ions were distinguished on the basis of their distance to hole-trapping oxide defects. Valence switching was found to be reversible. Slow ionization of Sm^{2+} occurred in the dark *via* tunneling. Additionally, Sm^{2+} could be photoionized using light of appropriate wavelength *via* injection into the host's conduction band. Wavelength-dependent photoionization studies enabled construction of a host-referred binding energy diagram of photogenerated Sm^{2+} in BaFBr. Findings reported herein enlarge the library of photoexcitable storage nanophosphors based on alkaline-earth fluorohalides.

Introduction

Storage phosphors are photosensitive materials in which information may be written, read, and erased using light. Two types of phosphors ought to be distinguished: photostimulable and photoexcitable. Photostimulable phosphors are well-known and ubiquitous in X-ray radiography. In these phosphors, electron–hole pairs created upon interaction with X-rays are trapped in metastable centers thus creating a latent image.[1] An intrinsic limitation of these materials as optical storage media is the destructive nature of the readout process, which entails emptying electron and hole traps. By contrast, photoexcitable phosphors are a class of storage phosphors in which exposure to X-ray or UVC radiation leads to stable luminescent centers.[2–10] This allows for nondestructive readout by probing their photoluminescence response. This is a key advantage of photoexcitable phosphors that underpins their potential as optical storage media in dosimetry,[2,5,6,8,11] multilevel data storage,[3,9,12] and anticounterfeiting.[13]

Rare-earth-doped alkaline earth fluorohalides of formula MFX:RE (M = Ca, Sr, Ba; X = Cl, Br, I; RE = rare-earth) are

well-established photostimulable phosphors. BaFBr:Eu^{2+}, for example, has been the archetypical X-ray storage phosphor for more than four decades. More recent is the demonstration that this family of materials may serve as photoexcitable phosphors.[2,14] Storage relies on reversible valence switching of a trivalent rare-earth activator doped into the fluorohalide host. Photoreduction of the rare-earth to its divalent state (RE^{3+} → RE^{2+}) occurs upon exposure to X-ray or UVC radiation and constitutes a write operation. A read operation is performed by probing the photoluminescence of radiation-generated ions ([RE^{2+}]* → RE^{2+}), which may be excited using UVA/B or visible light. Finally, an erase operation entails using high-power illumination to bleach divalent ions *via* photoionization (RE^{2+} → RE^{3+}). The functionality of alkaline-earth fluorohalides as photoexcitable storage phosphors relies on two distinct chemical units; these are electron-trapping trivalent rare-earth ions and hole-trapping oxide defects.[3,4] Unlike rare-earth doping, oxygen doping is unintentional but unavoidable.[15–18] Oxygen enters the anionic substructure as oxygen–halogen vacancy pairs, which result from substitution for fluorine or halogen and creation of a charge-compensating halide vacancy $\left(O'_{F/X} - v^{\bullet}_X\right)$.[15,18–21] Negatively charged oxide defects are able to store holes,[15,16,19] while positively charged

Department of Chemistry, Wayne State University, Detroit, MI 48202, USA.
E-mail: far@chem.wayne.edu

halide vacancies may serve as electron traps (*i.e.*, F color centers $F(X^-)$). Although the involvement of color centers in the storage mechanism of photostimulable phosphors is well established,[15,22–24] their role in the dynamics of electron trapping in photoexcitable phosphors remains an open question.[4,5,8,25]

To the best of our knowledge, the library of alkaline-earth fluorohalides that have been shown to serve as photoexcitable storage phosphors is limited to BaFCl doped with Sm^{3+}. Riesen and coworkers have generated a body of research centered on the X-ray- and UVC-induced valence switching in that system,[2,3,7,12,13,25–28] even though they also reported the feasibility of using Tm^{3+} as a photoreducible dopant.[4] Likewise, studies from Zhang's group have focused on BaFCl:Sm^{3+}, although in this case valence manipulation was accomplished through femtosecond-pulsed IR radiation.[29–31] The focus on BaFCl as a host likely stems from the fact that this was the composition first studied by Riesen and Kaczmarek in 2007.[2] The choice of trivalent samarium as an activator and electron trap is due to historical reasons too—BaFCl:Sm has been extensively studied as a spectral hole burning material[32]—but also to the distinct electronic structure of its divalent ion. Dieke diagrams for Sm^{3+} and Sm^{2+} are given in Fig. 1. The close proximity of Sm^{2+} excited states $4f^6$ (^5D_J) and $4f^55d^1$ directly affects photoluminescence and photoionization processes. Further, since the position of the $4f^55d^1$ state depends on the local crystal field, the host's composition may be used as a lever to exercise synthetic control over those processes. Besides chemical composition, investigations from Riesen's and Zhang's groups shared the use of nanocrystalline BaFCl:Sm^{3+} prepared *via* coprecipitation as the photosensitive material. Strictly speaking, they used submicron-sized crystals featuring only one dimension in the nanoscale regime (<100 nm). Riesen's studies have indicated that transitioning from bulk to nanophosphors positively impacts a number of aspects of photosensitive response, including higher storage density (due to a higher concentration of defects) and reduced energy consumption (due to lower bleaching thresholds).[2,3,12,26]

However, the size dependence of this response remains to be established.

Research opportunities that emerge from this brief review of the literature include expanding the library of photosensitive fluorohalide compositions and improving morphological control of nanocrystalline fluorohalides. As an example, BaFBr:Sm^{3+} is a remarkable absence in the library of photoexcitable phosphors, especially considering that its Eu^{2+}-doped counterpart is the archetypical photostimulable phosphor. Likewise, colloidal routes to fluorohalide nanocrystals are absent from the synthetic toolbox, despite the fact that they could afford much better control over size and size distribution than coprecipitation. Expanding the compositional library and achieving morphological control would enlarge the knowledge base to derive composition–structure–photosensitivity while capitalizing functional advantages resulting from crystal size reduction. In this article, we leverage our group's expertise in the synthesis[33] and structural analysis[34] of nanocrystalline rare-earth-doped fluorohalides to address those two gaps in the field of photoexcitable storage phosphors. We report an investigation of the UVC-induced valence switching in monodisperse BaFBr:Sm^{3+} nanocrystals synthesized *via* hot-injection of metal difluorobromoacetates. Steady-state, time-resolved, and variable-temperature luminescence studies were conducted to characterize the nanophosphors' photochemical response. The extent and kinetics of Sm^{3+} photoreduction and the stability of photogenerated Sm^{2+} were quantitatively analyzed with the aim of understanding the interplay between charge carrier traps, including the structural bases of this interplay. Energy levels of Sm^{2+} were mapped and their location within the bandgap of BaFBr estimated with an eye towards identifying optimum wavelengths to excite photoluminescence and induce photoionization.

Experimental

Synthesis of BaFBr:Sm^{3+} nanocrystals

Nanocrystal synthesis was conducted using standard Schlenk techniques under nitrogen atmosphere. $BaCO_3$ (99.98%), Sm_2O_3 (99.9%), CF_3COOH (99%), $CF_2BrCOOH$ (97%), oleic acid (90%), 1-octadecene (90%), and trioctylphosphine (97%) were used as reagents. All reagents were purchased from Sigma-Aldrich except $CF_2BrCOOH$, which was purchased from Synquest Laboratories. Chemicals were used as received. CF_3COOH, $CF_2BrCOOH$, and trioctylphosphine were stored under N_2. BaFBr:Sm^{3+} (4 mol%) nanocrystals were synthesized following a modified hot-injection route previously reported by our group.[33] This approach entailed preparation of metal bromodifluoroacetate precursors followed by thermolysis in a mixture of high-boiling point organic solvents. Metal precursors were synthesized *via* solvent evaporation.[35] $BaCO_3$ (0.96 mmol) and Sm_2O_3 (0.02 mmol) were added to a 50 mL two-neck round-bottom flask containing 1 mL of CF_3COOH and 5 mL of double-deionized H_2O. The resulting mixture was heated at 65 °C for 12 h until a colorless and optically transparent solution was

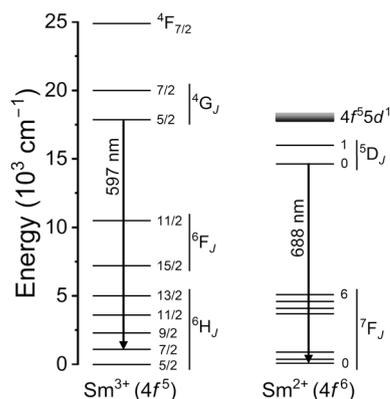**Fig. 1** Dieke diagrams of Sm^{3+} and Sm^{2+}. For the latter, the position of the lowest level of the $4f^55d^1$ excited state corresponds to that derived in this work for BaFBr and overlaps with that of the $4f^6$ $^5D_2$ level ($\approx 17\,800$ cm^{-1}, not shown).

obtained. Then, 2 mmol of $CF_2BrCOOH$ were added to the solution and stirred until fully dissolved. Polycrystalline precursors were obtained by evaporating the solution at 65 °C for 48 h under a constant flow of nitrogen (200 mL min^{-1}). Once evaporation was completed, 2 mL of oleic acid and 2 mL of octadecene were added to the flask containing the metal precursors. The flask was immersed in a sand bath and heated to 115 °C under vacuum for 45 min; magnetic stirring was used throughout. Then, the atmosphere was switched to nitrogen and the temperature of the sand bath increased to 140 °C. The solution was kept 5 min at that temperature and then injected into a 100 mL two-neck round-bottom flask containing 8 mL of trioctylphosphine at 300 °C under nitrogen atmosphere. A needle thermocouple was in direct contact with the reaction mixture. The temperature drop upon injecting all 4 mL of the precursor solution was ≈43–45 °C. The reaction proceeded for 20 min after injection. Then, the flask containing the reaction mixture was quenched to room temperature using a stream of air; a yellowish turbid solution was thus obtained. Nanocrystals were isolated by adding 80 mL of ethanol (200 proof), vortexing for 5 s, and then centrifuging at 8000 rpm for 10 min. The resulting precipitate was resuspended by adding a mixture of 7 mL of ethanol, 2 mL of methanol, and 5 mL of toluene and vortexing for 1 min. Centrifugation at 8000 rpm for 10 min and vacuum drying at room temperature concluded the work-up process. In a typical synthesis, ≈160–175 mg of polycrystalline BaFBr:Sm^{3+} were obtained (≈68–75% yield). The Sm/Ba molar ratio determined by ICP–OES (Galbraith Laboratories) was 0.0331, corresponding to a doping efficiency of 80%. Polycrystalline samples appeared off-white in color and were employed in chemical, structural, morphological, and luminescence studies.

Powder X-ray diffraction (PXRD)

PXRD patterns were collected using a Bruker D2 Phaser diffractometer operated at 30 kV and 10 mA. Cu Kα radiation (λ = 1.5418 Å) was employed. A nickel filter was used to remove Cu Kβ radiation. Diffractograms were collected in the 10–60° 2θ range using a step size of 0.012° and a step time of 1 s.

Rietveld analysis

Rietveld analysis[36,37] of PXRD data was conducted using GSAS-II.[38] The following parameters were refined: (1) scale factor and sample displacement; (2) background, which was modeled using a shifted Chebyschev polynomial function; (3) lattice constants; (4) atomic coordinates when allowed by space-group symmetry ($P4/nmm$); and (5) crystallite size and microstrain. Isotropic displacement parameters were fixed at 0.01, 0.03, and 0.02 Å^2 for Ba, F, and Br, respectively. Difference curve and R_w residual were employed to assess the quality of the refined structural model.

Transmission electron imaging (TEM)

TEM images were obtained using a Thermo Scientific Talos F200X G2 S/TEM microscope operated at 200 kV. A small aliquot of the native solution containing BaFBr:Sm^{3+} nanocrystals was mixed with toluene and dropcast onto a 200 mesh Cu grid coated with a Lacey carbon film (Ted Pella Inc.). Size distribution histograms were obtained after analyzing 150 nanocrystals.
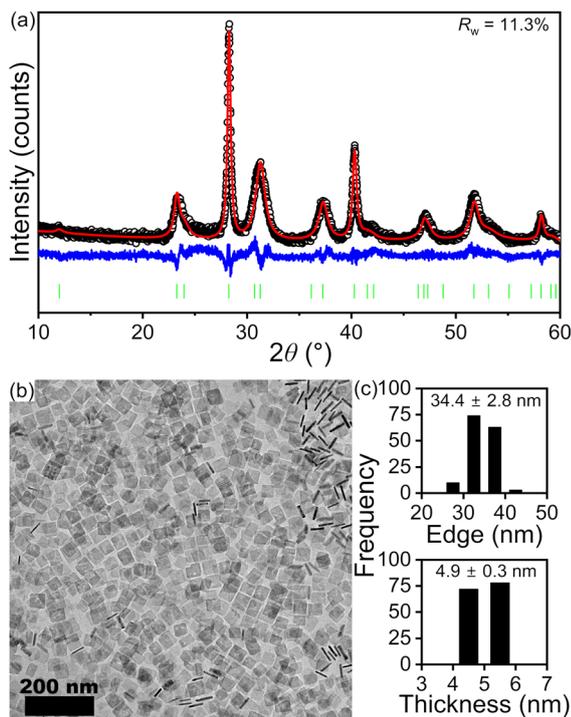
Spectrofluorometry

Spectrofluorometric analyses were conducted using a Fluorolog 3–222 fluorometer (Horiba Scientific). Steady-state spectra were collected using a 450 W xenon lamp and a variety of continuous-wave laser diodes (375, 405, 425, and 442 nm) as excitation sources. The 405 nm laser diode was operated in pulsed mode to collect time-resolved decays. A photomultiplier tube R928 served as the detector. UVC radiation from a 185 nm U-shaped lamp (49 uW cm^{-2} at 10 cm, Rexim, LLC) was used to induce photoreduction of Sm^{3+} to Sm^{2+}. Photoreduction, photoluminescence, and photoionization experiments were conducted on polycrystalline BaFBr:Sm^{3+} loaded into a VPF–800 cryostat (Lake Shore Cryotronics), which allowed data collection at atmospheric and low pressures (<30 mTorr) and variable temperatures (80–800 K). The stage was equipped with a custom-made sample holder featuring a copper block with a 12×0.8 mm cavity (diameter × depth). The sample was held in place by a fluorescence-free UV-grade fused-silica window secured by a stainless-steel retainer and four spring-loaded screws. The UVC lamp was located outside the cryostat at ≈6 cm from the sample surface. Dynamic vacuum was monitored using a convection-enhanced Pirani gauge (Kurt J. Lesker, model KJL275807LL). Sample temperature was probed using a thermocouple directly connected to the copper holder and a cryogenic controller (Lake Shore Cryotronics, model 335 − 3060). Spectra and decays were collected with a bandpass of 2 nm.

Results and discussion

The phase purity and morphology of BaFBr:Sm^{3+} nanocrystals were probed using PXRD and TEM, respectively. A PXRD pattern and a representative TEM image are given in Fig. 2 along with nanocrystal size distribution histograms. Rietveld analysis confirmed the phase purity of polycrystalline BaFBr:Sm^{3+} as all diffraction maxima in the pattern were indexed to the fluorobromide phase (PDF No. 024–0090); no secondary crystalline phases were observed (Fig. 2a). Refined unit cell constants, atomic coordinates, and bond distances are given in the SI (see Table S1). Diffraction maxima exhibited anisotropic microstrain broadening that complicated adequate modeling of (101), (002), and (111) reflections (2θ ≈ 23.3°, 23.9°, and 30.7°, respectively). From a morphological standpoint, nanocrystals consisted of square plates with an average edge length of 34.4 nm and an average thickness of 4.9 nm (Fig. 2b and c; see Fig. S1 in SI for additional TEM images). Important in the context of this research is the observation that polydispersities below 10% were achieved in both dimensions. Such a narrow size distribution—i.e., monodisperse nanocrystals—is ideal to maximize the statistical significance of structure–photophysics and structure–photochemistry relationships
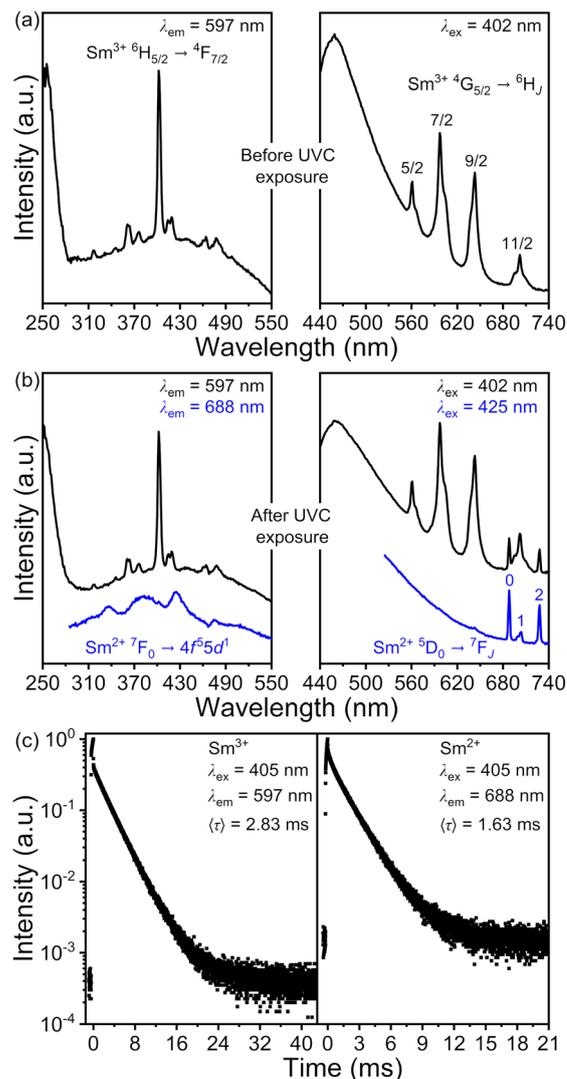
Fig. 2 (a) Rietveld analysis of the PXRD pattern of BaFBr:Sm^{3+}. Experimental (○) and calculated patterns (—), difference curve (—, offset for clarity), and tick marks (|) corresponding to the calculated positions of the diffraction maxima are shown. (b) Representative TEM image showing nanoplates in two different orientations: base-lying and side-lying. (c) Size distribution histograms obtained after measuring 150 nanoplates.

derived from probing the nanocrystal ensemble. The size distribution reported herein for BaFBr:Sm^{3+} is significantly narrower than in our previous report of rare-earth-doped BaFBr nanocrystals synthesized *via* hot-injection, for which the polydispersity was 28%.[33] We attribute this result to the combination of two synthetic modifications that delayed the beginning of Ostwald ripening (*i.e.*, size defocusing); these were (i) injection of a larger volume of precursor solution (4 mL *vs.* 2 mL) at a much faster rate (2 s *vs.* 2 min), and (ii) heating the precursor solution to a higher temperature prior to injection (140 °C *vs.* 115 °C). Results from electron microscopy imaging confirmed the ability of hot-injection synthesis to afford significantly better morphological control than coprecipitation routes previously employed in the preparation of BaFCl:Sm^{3+}. Although coprecipitation yielded plate-shaped fluorochloride crystals, their sizes were significantly larger than that of our monodisperse fluorobromide nanoplates (*e.g.*, 300 × 200 × 70 nm^3 and 600 × 400 × 90 nm^3 *vs.* 34 × 34 × 5 nm^3);[2,13,25] moreover, no information was provided regarding size distribution.

We then proceeded to screen the photoluminescence of as-prepared BaFBr:Sm^{3+} nanocrystals before and after exposure to UVC radiation. Results from those studies are summarized in Fig. 3. Excitation and emission spectra and time-resolved decays were collected at room temperature under ambient atmosphere. Bands arising from f–f radiative transitions of Sm^{3+} and from oxide defects were observed before UVC

Fig. 3 (a) and (b) Excitation and emission spectra of BaFBr:Sm^{3+} before and after exposure to UVC radiation under ambient atmosphere. Relevant transitions of Sm^{3+} and Sm^{2+} are labeled. (c) Time-resolved luminescence decays of Sm^{3+} and Sm^{2+} collected after UVC exposure. Intensity-weighted average lifetimes are given.

exposure (Fig. 3a). Sm^{3+}-centered transitions appeared in the excitation spectrum ($^6H_{5/2} \rightarrow {}^4F_{7/2}$, 402 nm) as well as in the emission spectrum ($^4G_{5/2} \rightarrow {}^6H_J$, J = 5/2 at 561 nm, 7/2 at 597 nm, 9/2 at 643 nm, and 11/2 at 702 nm). Emission bands sat on a broad background likely arising from oxide defects, whose emission peaked at 458 nm. Sm^{3+} emission was observed upon direct f–f excitation at 402 nm and upon charge-transfer excitation of oxide defects at 250 nm (O^{2-} + Sm^{3+} ($^6H_{5/2}$) → O$^-$ + Sm^{2+} ($^7F_0$)). Oxide defects in BaFCl and BaFBr are well-known to absorb at 250 nm and below.[3,15,18,20,39] Exposure of BaFBr:Sm^{3+} nanocrystals to UVC radiation (185 nm, 6.7 eV) for a few minutes led to partial photoreduction of Sm^{3+} to Sm^{2+}, as demonstrated by the appearance of emission bands arising from f–f radiative transitions of the divalent ion (Fig. 3b, $^5D_0 \rightarrow {}^7F_J$, J = 0 at 688 nm, 1 at 703 nm, and 2 at 727 nm). The observation that valence switching occurred under sub-bandgap

illumination (<8.3 eV)[40,41] pointed to photoinduced electron transfer from oxide defects (hole traps) to Sm^{3+} (electron traps) as the photoreduction reaction, similar to what has been reported by Riesen and coworkers for $BaFCl:Sm^{3+}$.[3] This hypothesis was further supported by the fact that Sm^{3+} could be photoreduced upon exposure to 250 nm radiation (4.96 eV), which matches the absorption of oxide defects (see SI, Fig. S2). From a structural standpoint, photoinduced electron transfer relies on the close proximity of the donor and the acceptor. X-ray absorption studies conducted by our group demonstrated that trivalent rare-earth ions doped into alkaline-earth fluoro-halides may indeed have oxide ions as nearest-neighbors;[34] a similar scenario had been considered previously by Liu and coworkers on the basis of post-synthetic annealing studies of coprecipitated $BaFCl:Sm^{3+}$.[42] Sm^{2+} emission was observed upon $4f^6 \, (^7F_0) \rightarrow 4f^5 5d^1$ excitation; the corresponding band extended from 285 to 550 nm and featured a maximum at 425 nm. The broadness of this band enabled simultaneous excitation of Sm^{2+} and Sm^{3+} at 402 nm or selective excitation of Sm^{2+} at 425 nm. The ability to excite both ions using a single wavelength close to 402 nm was important in the context of this research. As will be described below, we monitored the progress of photochemical reactions using two observables obtained upon laser excitation at 405 nm; these were emission intensities from Sm^{3+} (597 nm) and Sm^{2+} (688 nm) and their ratio. In fact, a 405 nm laser was used to collect time-resolved decays of Sm^{3+} at 597 nm ($^4G_{5/2} \rightarrow {}^6H_{7/2}$) and of Sm^{2+} at 688 nm ($^5D_0 \rightarrow {}^7F_0$). Intensity-weighted average lifetimes ($\langle\tau\rangle$) of their corresponding excited states were computed according to eqn 1, where $I(t)$ is the baseline-corrected luminescence intensity at time t, and t_i and t_f define the integration window.[43]

$$\langle\tau\rangle = \frac{\int_{t_i}^{t_f} I(t) t \, dt}{\int_{t_i}^{t_f} I(t) \, dt} \tag{1}$$

Integration was carried out from the first point of the decay until its return to the baseline level. Values of 2.83 and 1.63 ms were thus obtained for Sm^{3+} and photogenerated Sm^{2+}, respectively (Fig. 3c).

We decided to gain insight into the UVC-induced photochemistry of $BaFBr:Sm^{3+}$ nanoplates. Specifically, we were interested in probing a number of aspects that are relevant from the standpoint of optical storage, including photoreduction extent, kinetics, and reversibility, as well as stability of photogenerated Sm^{2+} ions. To this end, a series of experiments was conducted, the first of which was to study the photoreduction of $BaFBr:Sm^{3+}$ under ambient atmosphere (760 Torr, 22–25 °C, relative humidity = 22–26%) and under vacuum (5–30 mTorr, 22–25 °C). This experiment entailed following the photoreduction of Sm^{3+} under UVC illumination and the stability of the photogenerated Sm^{2+} in the dark as a function of time. Polycrystalline $BaFBr:Sm^{3+}$ was loaded into the cryostat, exposed to 185 nm UVC radiation, and emission spectra were collected over time. Spectra were excited using a 405 nm laser diode (3.1 mW), thereby allowing simultaneous excitation of Sm^{2+} and Sm^{3+} and extraction of the ratio between the
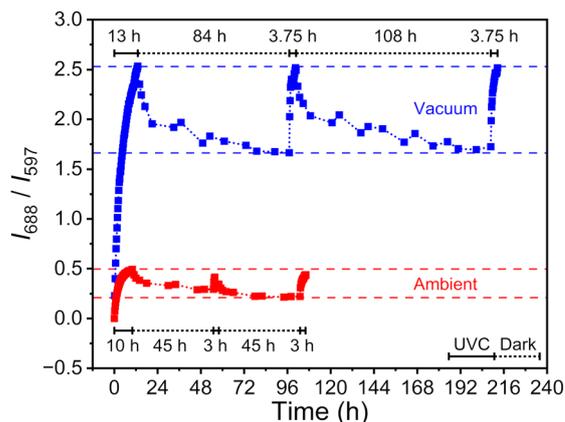

Fig. 4 Luminescence intensity ratio curves obtained upon subjecting $BaFBr:Sm^{3+}$ to UVC–dark cycles under ambient atmosphere and under vacuum. Ratios were computed by integrating emission bands at 597 (Sm^{3+}) and 688 nm (Sm^{2+}) between 582 and 614 nm and between 685 and 690 nm, respectively. Dashed and dotted lines are guides to the eye. UVC and dark exposure times are indicated.

integrated intensities of their main emission bands at 688 and 597 nm (I_{688}/I_{597}), respectively; the UVC lamp was blocked during acquisition of spectra. Once saturation was achieved and the intensity ratio remained unchanged, the UVC lamp was turned off, and the sample left in the dark. Then, emission spectra were collected until the intensity ratio remained constant; this marked the completion of a UVC–dark cycle. $BaFBr:Sm^{3+}$ solids were subjected to two consecutive UVC–dark cycles; a third exposure to UVC radiation was carried out to check repeatability. Intensity ratio vs. time curves were thus obtained and are given in Fig. 4; the time evolution of the corresponding integrated intensities is given in the SI (Fig. S3). Intensity ratio curves obtained under ambient atmosphere and under vacuum exhibited similar shape. The I_{688}/I_{597} ratio—a qualitative proxy for the extent of photoreduction—increased under UVC illumination due to the photoreduction of Sm^{3+} and decreased in the dark due to detrapping of electrons from photogenerated Sm^{2+} (i.e., dark ionization). The time evolution of the ratio was driven by the intensity of Sm^{2+} emission, which evolved in the exact same way. However, there were two major differences between the photochemical response of $BaFBr:Sm^{3+}$ under ambient atmosphere and under vacuum. The first difference involved the extent of photoreduction, which appeared to be larger under vacuum. A fivefold increase in the saturation intensity ratio was observed upon going from ambient ($I_{688}/I_{597} \approx 0.50$) to vacuum exposure ($I_{688}/I_{597} \approx 2.50$). The second difference involved the repeatability of the photochemical response, which was noticeably more consistent when conducting UVC–dark cycles under vacuum (i.e., the same saturation ratio was achieved three times). This difference stemmed from the evolution of Sm^{3+} emission, which was erratic under ambient atmosphere but repeatable under vacuum. Altogether, results from these studies provided two major lessons. The first lesson was that partial photoreduction of Sm^{3+} to Sm^{2+} was reversible and repeatable, more so under vacuum than under air. On this basis, we decided to conduct all

subsequent experiments under dynamic vacuum (<30 mTorr). The second lesson was that at least a fraction of photosensitive Sm^{3+} ions was likely located at or near the surface of the nanocrystals. Thus, their ability to participate in photochemical reactions and photoluminesce was impacted by the presence of chemisorbed ligands. For example, one may envision a Sm^{3+} ion that was not photoactive under air due to the presence of coordinated water or hydroxyl groups, but became coordinatively unsaturated under vacuum and thus more prone to photoreduction. The participation of surface Sm^{3+} ions in photochemical reactions was further supported by the larger response obtained upon thermally treating BaFBr:Sm^{3+} nanocrystals under vacuum (*vide infra*). Infrared spectroscopy showed that, indeed, vacuum and thermal treatment of BaFBr:Sm^{3+} nanoplates induced partial dehydration of their surfaces as well as removal of residual organics (see SI, Fig. S4). For completeness, we add that X-ray absorption studies conducted by our group demonstrated that the local atomic environment of trivalent rare-earth ions doped into fluorohalide nanocrystals is highly disordered, compatible with a surface or subsurface location.[34] Finally, the observation of electron detrapping in the dark raised the question of the kinetic stability of photogenerated Sm^{2+}. Studies aimed at addressing this aspect are described in the following paragraph.

Photoreduction under UVC illumination and ionization in the dark were further probed by monitoring the evolution of emission intensities over the course of a single UVC–dark cycle under vacuum. This study, however, featured two major differences with that described in the previous paragraph; these were (i) a larger number of emission spectra was acquired to get intensity *vs.* time curves suitable to extract kinetic information, and (ii) the 405 nm laser power was decreased to 0.5 mW to minimize optically induced detrapping (*i.e.*, photoionization of Sm^{2+} *via* excited-state tunneling to hole traps and/or through injection into the host's conduction band when allowed by trap depth). Completion of this experiment took ≈ 10 days and the corresponding results are given in Fig. 5; selected emission spectra are given in the SI (Fig. S5). The intensity ratio I_{688}/I_{597} followed the expected trend, reaching a saturation value of ≈ 2.60 after 17 h of UVC exposure and decreasing to ≈ 1.40 after leaving the sample in the dark for 226 h (Fig. 5a). Similar to what was described earlier, this trend was driven by the evolution of Sm^{2+} emission at 688 nm. It should be noted that the intensity of this emission decreased $\approx 45\%$ from its maximum value after *ca.* 9 days (Fig. 5b), thus limiting the use of our BaFBr:Sm^{3+} nanoplates as storage media. More importantly, the fact that extensive dark ionization was observed in monodisperse nanocrystals suggests that there may be a size limit to downscale photoexcitable storage phosphors without compromising functionality. With regards to Sm^{3+} emission at 597 nm, its evolution followed the expected trend during photoreduction, *i.e.*, it decreased with UVC exposure time. By contrast, two stages were noticeable in the I_{597} curve extracted after ceasing UVC illumination. First, an increase in emission intensity was observed during the first 12 h in the dark, indicating that
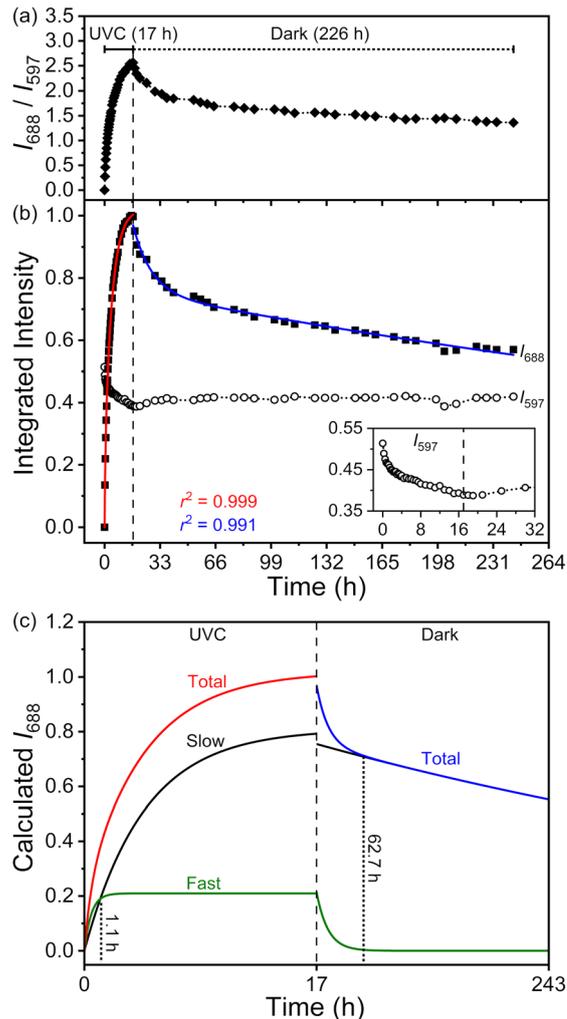

Fig. 5 Kinetics of UVC photoreduction and dark ionization of BaFBr:Sm^{3+} under vacuum. Time evolution of the luminescence intensity ratio (a) and of the corresponding integrated intensities I_{597} and I_{688} (b). A magnified view of the $I_{597}(t)$ curve is shown in the inset of (b). Fits of equations 2 and 3 to the $I_{688}(t)$ curve are shown as solid red and blue lines, respectively. Fit residuals are given. (c) $I_{688}(t)$ curve calculated according to eqn (4a) and (4b) (UVC stage) and eqn (5a) and (5b) (dark stage). Contributions from slow and fast components to the total intensity are plotted. Dashed and dotted lines are guides to the eye.

detrapping of electrons from Sm^{2+} generated luminescent Sm^{3+} ions. In the second stage, however, the intensity of Sm^{3+} emission remained practically constant even though dark ionization of Sm^{2+} occurred. Thus, detrapping took place without the generation of luminescent Sm^{3+} ions; a similar phenomenon was reported by Qin and coworkers in their study of photobleaching of BaF(Cl,Br):Sm^{2+}.[44] The time evolution of Sm^{2+} emission at 688 nm was quantitatively analyzed to extract rate constants for photoreduction and dark ionization. Previous kinetic studies of carrier trapping and detrapping in Sm-doped fluorides[6,8] and fluorohalides[3,25,27,44] had shown these processes to be dispersive. In the case of our BaFBr:Sm^{3+} nanoplates, we fitted the $I_{688}(t)$ curve using biexponential functions given in eqn (2) (photoreduction stage,

t = 0–17 h) and eqn (3) (dark stage, t = 17–243 h).[27] Here a is a scaling factor, f and $(1 - f)$ are the fractions of the two distinct

$$\text{Photoreduction: } I_{688}(t) = a\{1 - f\exp[-k_1(t - t_0)]$$
$$- (1 - f)\exp[-k_2(t - t_0)]\} \qquad (2)$$

$$\text{Dark: } I_{688}(t) = a\{f\exp[-k_1(t - t_0)] + (1 - f)\exp[-k_2(t - t_0)]\} \qquad (3)$$

Sm^{2+} emitters, k_1 and k_2 their corresponding rate constants, and t_0 a time shift. Adequate fits were obtained for both stages (Fig. 5b). Parameter values extracted for the photoreduction stage were a = 1.019(3), f = 0.794(7), k_1 = 0.229(4) h^{-1}, and k_2 = 2.0(1) h^{-1}. Values for the dark stage were a = 0.969(7), f = 0.221(8), k_1 = 0.09(1) h^{-1}, and k_2 = 0.00138(7) h^{-1}. These values revealed that Sm^{2+} emission in both stages stemmed from a major slow component ($\approx$ 80%) and a minor fast component ($\approx$ 20%). This scenario was better visualized by plotting the individual contributions of each component ($I_{slow}(t)$ and $I_{fast}(t)$) to the total emission intensity ($I_{688}(t) = I_{slow}(t) + I_{fast}(t)$). These contributions were calculated using eqn (4a) and (4b) (photoreduction stage) and eqn (5a) and (5b) (dark stage).

$$\text{Photoreduction: } I_{slow}(t) = af[1 - \exp(-k_1t)] \qquad (4a)$$

$$I_{fast}(t) = a(1 - f)[1 - \exp(-k_2t)] \qquad (4b)$$

$$\text{Dark: } I_{slow}(t) = a(1 - f)\exp(-k_2t) \qquad (5a)$$

$$I_{fast}(t) = af\exp(-k_1t) \qquad (5b)$$

Inspection of $I_{slow}(t)$ and $I_{fast}(t)$ curves thus derived showed that the photogeneration of Sm^{2+} was dominated by the fast component for the first hour under UVC illumination (Fig. 5c). At that point, the slow component became dominant and the fast component no longer contributed to the increase of the total emission intensity at 688 nm. Likewise, dark ionization was initially dominated by the fast component, which accounted for most of the $\approx$ 30% intensity drop observed within the first 46 h in the dark. At the end of that period, emission from the fast component was negligible and the decrease in the intensity at 688 nm was entirely due to the decay of the slow component. It is worth noting that fast detrapping from Sm^{2+} coincided in time with the partial recovery of the Sm^{3+} emission at 597 nm, whereas slow detrapping did not generate luminescent Sm^{3+} ions. For completeness, we also note that the time evolution of the emission decay from the slow component was quasilinear within the time window considered (17–243 h). In fact, a linear fit of this curve yielded a fit residual equal to 0.998 and a decay rate equal to 0.089% h^{-1} (0.999 and 0.086% h^{-1}, respectively, were obtained when the fit was conducted between 63 and 243 h). The biexponential kinetics of electron trapping (photoreduction) and detrapping (dark ionization) and the fact that the fractions of each component were the same in both processes pointed to a bimodal distribution of photoactive Sm^{3+} centers within the nanocrystals.

From a structural standpoint, two types of Sm^{3+} ions could be distinguished on the basis of their proximity to oxide

defects. The first type of Sm^{3+} centers (type I) consisted of those having oxide defects in close proximity so that exposure to UVC radiation favored direct $O^{2-} \rightarrow Sm^{3+}$ electron transfer and caused fast photoreduction of Sm^{3+}. Dark ionization of the photogenerated Sm^{2+} occurred via direct electron backtransfer or short-distance tunneling and quickly restored the luminescence of the parent Sm^{3+}. The local structure of type I Sm^{3+} was rather static since the same photochemical response was observed upon UVC–dark cycling. The second type of Sm^{3+} centers (type II) involved those having oxide defects at a longer distance, such that photoreduction via direct electron transfer was not feasible. It is worth recalling that oxygen typically enters the fluorohalide lattice as oxide–halide ion vacancy pairs and that these defect pairs may act as hole–electron traps under X-ray or UVC radiation.[15,18] We propose that UVC exposure led to photoexcitation of these pairs via formation of O^- and a neutral color center ($F(X^-)$), followed by slow diffusion of the latter through the fluorohalide lattice to generate Sm^{2+} via reaction with a type II Sm^{3+} ($F(X^-) + Sm^{3+} \rightarrow v_X^\bullet + Sm^{2+}$). This reaction bleached Sm^{3+} centers that were initially luminescent. Photodissociation of oxide–halide ion vacancy pairs and diffusion of the resulting color centers is a key piece underlying the functionality of photostimulable BaFBr:Eu^{2+} phosphors.[15,23,24] Diffusion of carrier traps was also brought up in studies of BaFCl:Sm^{3+},[12] BaFCl:Tm^{3+},[4] BaLiF$_3$:Sm^{3+},[6] and CaF$_2$:Sm^{3+}.[8] It must be invoked here to rationalize the observation that the initial emission intensity from Sm^{3+} was not recovered after dark ionization following the first exposure to UVC radiation. In other words, the first exposure to UVC radiation caused an irreversible structural change that bleached Sm^{3+} centers that were initially luminescent. Thus, unlike the case of type I Sm^{3+}, a dynamic structural component appeared to be involved in the initial photoreduction of type II Sm^{3+}. Radiation-induced structural distortions were also observed in NaMgF$_3$:Sm.[45] Luminescent Sm^{2+} centers generated via diffusion of color centers underwent slow dark ionization to yield nonluminescent Sm^{3+} and regenerate distant O^{2-} hole traps via long-distance tunneling ($Sm^{2+} + O^- \rightarrow Sm^{3+} + O^{2-}$). For completeness we note that the bimodal distribution proposed here bears resemblance to that described by Eachus et al. for photostimulable centers in BaFBr:Eu^{2+},[21] as both rely on a distribution of distances between carrier traps to rationalize experimental results.

Kinetic studies of electron trapping and detrapping were followed by a series of experiments aimed at mapping the energy levels of photogenerated Sm^{2+} centers. Specifically, we sought to establish the location of the 4f^{5}5d^1 excited state relative to the 4f^6 ^{7}F$_0$ ground state and to the bottom of the host's conduction band. The 4f^{5}5d^1 excited state is directly involved in the photophysical and photochemical response of Sm^{2+} because it (i) acts as a feeding state for 4f^6 ^{5}D$_J$ levels and impacts ^{5}D$_J \rightarrow$ ^{7}F$_0$ radiative processes through 4f–5d electronic mixing,[46–51] (ii) participates in the nonradiative depopulation of ^{5}D$_J$ levels through thermally activated ^{5}D$_J \rightarrow$ 4f^{5}5d^1 crossover,[46,48–50] and (iii) impacts the stability of photogenerated Sm^{2+} by serving as an intermediate state during photoionization (via ground-state absorption followed by excited-state tunneling

to hole traps or through excited-state absorption to the conduction band)[3,52] and photothermal ionization (ground state absorption followed by thermal injection into the conduction band).[53] Our strategy to establish the position of the $4f^5 5d^1$ excited state relative to the $^7F_0$ ground state was that described by Pal *et al.*[50] and Shen and Bray.[49] This approach entailed probing and modeling the temperature dependence of the lifetime corresponding to the $^5D_1 \rightarrow {}^7F_0$ radiative decay at 629 nm (15 898 cm^{-1}). To this end, steady-state emission spectra and time-resolved decays excited at 405 nm were collected between 80 and 300 K under vacuum (<30 mTorr). For these experiments, we used BaFBr:Sm^{3+} nanocrystals that had been previously saturated under UVC illumination and subsequently left in the dark for several days (until $I_{688}/I_{597} \approx 1.6$). The corresponding results are given in Fig. 6. Emission from the $^5D_1 \rightarrow {}^7F_0$ transition could be observed in the entire temperature range (Fig. 6a). The corresponding peak at 629 nm sat on a decreasing background. At room temperature, its intensity was very weak and it appeared as a shoulder of the Sm^{3+} $^4G_{5/2} \rightarrow {}^6H_{9/2}$ emission band centered at 642 nm. Time-resolved decays collected in 20 K increments were fit using a triexponential function given in eqn (6). Here $I(t)$ is the luminescence intensity at time t, τ_i is the lifetime of i-th component, and A_i and A are constants. Fractional contributions

$$I(t) = \sum_{i=1}^{i=3} A_i \exp\left(-\frac{t}{\tau_i}\right) + A \qquad (6)$$

$$F_i = \frac{\tau_i A_i}{\sum_i \tau_i A_i} \qquad (7)$$

$$\langle \tau \rangle = \frac{\sum_i \tau_i^2 A_i}{\sum_i \tau_i A_i} \qquad (8)$$

F_i were computed according to eqn (7) and the intensity-weighted average lifetime $\langle \tau \rangle$ estimated using eqn (8). In this case, a multiexponential approach was preferred over integration because of the need to go beyond the average picture in order to extract the temperature dependence of the $^5D_1$ excited-state lifetime. Experimental decays and fits are given in the SI (Fig. S6). Decays were dominated by a major component with lifetimes in the $\approx$6–9 ms range (τ_1, see Fig. 6b). These values, however, were significantly larger than those expected for the $^5D_1$ excited state of Sm^{2+} doped into fluorohalide hosts, which should be in the submilisecond range.[46,49,50] In the case of the second component (τ_2), lifetime values ranged between $\approx$0.7 and 1.7 ms and did not show the temperature dependence expected for the $^5D_1$ excited state, whose lifetime is known to decrease with temperature until reaching a few hundreds or tens of microseconds near room temperature.[46,49,50] On the other hand, lifetimes extracted for the third component (τ_3) were compatible with those expected for the $^5D_1$ excited state, both in terms of magnitude and temperature dependence; thus, τ_3 values are denoted $\tau(^5D_1)$ hereafter. $\tau(^5D_1)$ ranged from 140 μs at 80 K to 23 μs at 300 K; lifetime values were constant up to 180 K,
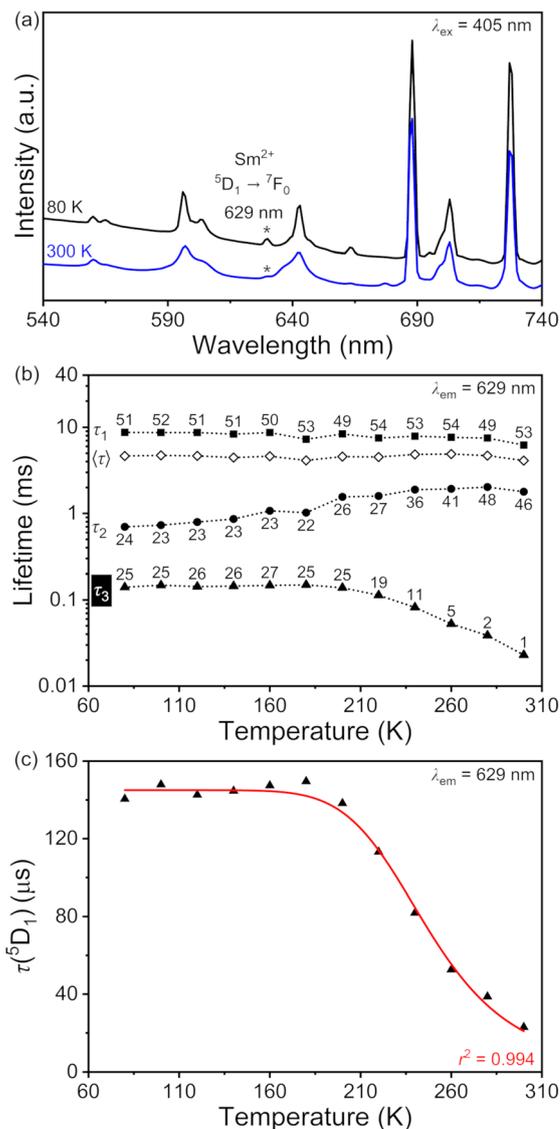

Fig. 6 (a) Emission spectra of BaFBr:Sm$^{2+/3+}$ at 80 and 300 K. Emission from the $^5D_1 \rightarrow {}^7F_0$ decay of Sm^{2+} at 629 nm is depicted with the * symbol. (b) Results from triexponential fits of variable-temperature time-resolved luminescence decays at 629 nm. Lifetimes and fractional contributions (%) are given for each component along with the intensity-weighted average lifetime. τ_3 corresponds to the lifetime of the $^5D_1$ level of Sm^{2+} ($\tau(^5D_1)$). Dotted lines are guides to the eye. (c) Temperature dependence of $\tau(^5D_1)$. Fit of eqn (9) to experimental lifetimes is depicted as a solid red line. Fit residual is given.

where the onset of thermal quenching was observed (Fig. 6c). Although Pal *et al.* observed the onset of thermal quenching at a similar temperature (*ca.* 200 K), the shape of their $\tau(^5D_1)$ *vs.* temperature curve differed from ours. Three temperature regimes were clearly noticeable in their case: constant lifetimes below 100 K ($\approx$800 μs) were followed by a moderate decrease up 200 K ($\approx$700 μs) and exhibited a drastic decrease upon going to 300 K ($\approx$40 μs).[50] A qualitatively similar three-temperature regime was reported by Shen and Bray for SrFCl:Sm^{2+}.[49] Quantitative insight into the temperature dependence of the $^5D_1$ level

was gained by fitting eqn (9) to the

$$\tau(^5D_1)(T) = \left[K_R + K_{10}\left[1 - \exp\left(\frac{-\Delta E_{10}}{pkT}\right)\right]^{-p} + K_{1fd}\exp\left(\frac{-\Delta E_{1fd}}{kT}\right)\right]^{-1}$$

(9)

experimental $\tau(^5D_1)(T)$ curve. This model accounts for depopulation of the excited state *via* one radiative channel ($^5D_1 \rightarrow {}^7F_0$ emission) and two nonradiative channels ($^5D_1 \rightarrow {}^5D_0$ multiphonon relaxation and $^5D_1 \rightarrow 4f^55d^1$ thermally-activated crossover).[46,49,50,54] Here, K_R is the radiative constant, K_{10} is the spontaneous multiphonon emission rate, ΔE_{10} is the energy gap between the $^5D_1$ and $^5D_0$ levels, and p is the number of phonons needed to bridge that gap. In the crossover term, K_{1fd} is a frequency factor and ΔE_{1fd} is the energy gap between the $^5D_1$ level and the lowest level of the $4f^55d^1$ excited state. The best fit was obtained by setting $K_R = 6897$ s^{-1} (based on a radiative lifetime equal to 145 μs), $\Delta E_{10} = 1363$ cm^{-1}, and $p = 5.7$ (based on an effective phonon frequency equal to 240 cm^{-1}).[55] Doing so, yielded $K_{10} = 0(50)$ s^{-1}, $K_{1fd} = 1.97(1.80) \times 10^8$ s^{-1}, and $\Delta E_{1fd} = 1768(163)$ cm^{-1} as refined parameters and $r^2 = 0.994$ as the fit residual. The zero value obtained for the multiphonon relaxation constant K_{10} reflected the negligible contribution of this nonradiative process to the depopulation of the $^5D_1$ level; a similar result was reported by He *et al.* in their study of BaCl$_2$:Sm^{2+}.[54] In the case of Pal *et al.*'s study of BaFBr:Sm^{2+}, inclusion of the multiphonon relaxation term was needed to adequately model the three temperature regimes observed in the $\tau(^5D_1)(T)$ curve.[50] The value of 1768 cm^{-1} obtained for the $^5D_1$–$4f^55d^1$ gap implied that the lowest level of $4f^55d^1$ excited state of Sm^{2+} was located 3131 cm^{-1} (0.39 eV) above the $^5D_0$ level and 17 666 cm^{-1} (2.19 eV) above the $^7F_0$ ground state. This estimate was in excellent agreement with that reported by Cui and coworkers based on variable-temperature steady-state spectra of BaFBr:Sm^{2+} (17 860 cm^{-1}, 2.21 eV)[56] but lower than that reported by Pal and coworkers (18 469 cm^{-1}, 2.29 eV).[50]

The energy of the $4f^55d^1$ excited state of Sm^{2+} relative to the $^7F_0$ ground state was subsequently used to estimate the gap between the $4f^55d^1$ state and the bottom of the host's conduction band (CB). This was accomplished by irradiating BaFBr:Sm$^{2+/3+}$ nanocrystals with laser light of decreasing energy until photoionization of Sm^{2+} was no longer observed due to the inability to bridge the $^7F_0$–CB gap. In these experiments, BaFBr:Sm^{3+} was first exposed to UVC radiation to generate Sm^{2+} ($I_{688}/I_{597} \approx 3.20$), and then continuously to laser light of fixed wavelength for 2 h. 375, 405, and 442 nm were used as wavelengths ($\lambda_{exposure}$), corresponding to energies equal to 3.31, 3.06, and 2.81 eV, respectively; in all three cases, the laser power was fixed at 0.5 mW. Emission spectra were collected before and after laser exposure using 405 nm excitation (0.5 mW). Photoionization experiments were conducted under vacuum using BaFBr:Sm^{3+} nanocrystals that had been thermally treated at 450 K for 6 h in the cryostat. These nanocrystals exhibited a photochemical response that was qualitatively similar to their as-prepared counterparts (see SI, Fig. S7 and S8). However, from a quantitative standpoint, two differences

should be pointed out. First, the extent of photoreduction appeared to be larger in thermally treated samples judging from the saturation intensity ratio ($I_{688}/I_{597} \approx 3.70$ *vs.* 2.50 in as-prepared nanocrystals). Additionally, dark ionization was slower judging from the percent change in the Sm^{2+} emission intensity ($\Delta I_{688} \approx -4\%$ in the first 2 h after ceasing UVC exposure *vs.* −9% in as-prepared nanocrystals). The increase in reaction extent upon going from as-prepared samples under air and vacuum to thermally treated samples confirmed that at least a fraction of the photoactive Sm^{3+} centers was located at or near the nanocrystals' surface. Slower dark ionization enabled probing photoionization of a larger population of Sm^{2+} centers. For completeness, we note that PXRD and thermal analyses demonstrated that treatment at 450 K did not impact the structural integrity of the nanocrystals (see SI, Fig. S9). Results from photoionization experiments are summarized in Fig. 7. Emission spectra shown therein are baseline-subtracted; raw spectra are given in the SI (Fig. S10). Exposure to 375 and 405 nm light caused a decrease of 47 and 30%, respectively, in the integrated intensity of the 688 nm band of Sm^{2+}. Thus, ionization of Sm^{2+} *via* excitation into the conduction band

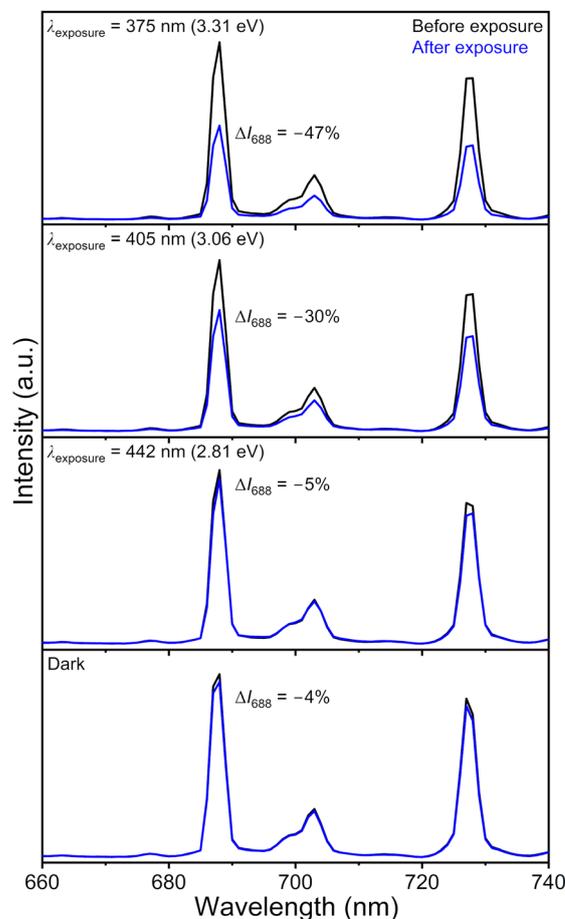**Fig. 7** Emission spectra of BaFBr:Sm$^{2+/3+}$ before and after exposure to laser light of wavelength $\lambda_{exposure}$. Spectra were collected using 405 nm excitation. The percent change of Sm^{2+} emission intensity at 688 nm (ΔI_{688}) is given.

occurred in these cases. By contrast, the decrease observed upon exposure to 442 nm light was comparable to that observed in the dark ($\Delta I_{688} \approx -5\%$), indicating that no light-induced detrapping took place. On this basis, the upper and lower limits for the $4f^5 5d^1$–CB gap were estimated using the energies corresponding to 405 and 442 nm photons as trap depths and that of the $^7F_0$–$4f^5 5d^1$ gap (2.19 eV); values of 0.87 (3.06–2.19) and 0.62 (2.81–2.19) eV were thus obtained.

Energy differences were used to construct a host-referred binding energy (HRBE) diagram of photogenerated Sm^{2+} in BaFBr:Sm^{3+} nanoplates; it is given in Fig. 8. The diagram was built using a value of 8.3 eV for the bandgap of BaFBr[40,41] and 0.87 eV for the $4f^5 5d^1$–CB gap. The $^7F_0$ ground state of Sm^{2+} was placed 2.19 eV below the $4f^5 5d^1$ excited state. We tentatively placed oxide defect levels 4.96 eV below Sm^{2+} $^7F_0$ level based on the observation of an $O^{2-} \rightarrow Sm^{3+}$ charge-transfer band at 250 nm; the energy of this excitation provided a means of estimating the ground state of photogenerated Sm^{2+} ions. Color centers were not included in the HRBE diagram but literature reports had placed them ≈ 2–2.5 eV below the bottom of BaFBr's conduction band.[22,57,58] The diagram is an average depiction of the position of energy levels within the host's bandgap. Nonetheless, it is informative from the standpoint of exploring the functionality of BaFBr:Sm^{3+} nanoplates as optical storage media. Specifically, it provides insight into how to approach reading and erasing Sm^{2+} centers generated upon UVC exposure. With regards to reading, one ideally wants to photoexcite Sm^{2+} without causing bleaching. From this perspective, results presented herein show that using light of wavelength longer than 405 nm is desirable if one is interested in probing Sm^{2+} emission intensities only. If excitation at 405 nm is used because the Sm^{2+}/Sm^{3+} luminescence intensity ratio is of interest, then very low powers ($\ll 0.5$ mW) should be employed to minimize optically induced detrapping. In the case of erasing, single-photon photoionization may be achieved using light of wavelength shorter than or equal to 405 nm. Increasing optical power increases the extent of photobleaching. As an example, a 72% decrease in the Sm^{2+} emission

intensity was achieved by exposing BaFBr:$Sm^{2+/3+}$ nanocrystals to 405 nm light of increasing power (up to 50 mW, see SI, Fig. S11). Multiphoton photoionization should also be possible using light of wavelength longer than 405 nm and $4f^6$ (^5D_J) and $4f^5 5d^1$ excited states as intermediates.[3,29] Finally, based on the HRBE diagram, one may envision photothermal ionization as an alternative for bleaching Sm^{2+} centers.[53] In principle, this could be accomplished by coupling ≈ 560 nm (2.2 eV) or shorter wavelength excitation to temperature. Then, optical population of the $4f^5 5d^1$ excited state would be followed by thermal depopulation *via* injection into the conduction band. This approach, however, could be limited by the highest temperature achievable without compromising the chemical and structural integrity of the nanoplates.

Conclusions

In summary, we showed that monodisperse BaFBr:Sm^{3+} nanoplates undergo reversible valence switching upon exposure to UVC radiation. Sm^{3+} and oxide defects served as electron and hole traps, respectively. The kinetics of photoreduction and dark ionization processes was rationalized invoking a bimodal distribution of photoactive Sm^{3+} centers, in which these were distinguished on the basis of their distance to oxide defects. One of these types of Sm^{3+} ions was permanently bleached after the first exposure to UVC radiation. We proposed that this was due to an irreversible structural change connected to the diffusion of color centers, which acted as transient electron traps. Results from photoionization studies served to estimate the depth of electron traps, which were found to be located between ≈ 2.8 and 3.1 eV below the bottom of the BaFBr host's conduction band.
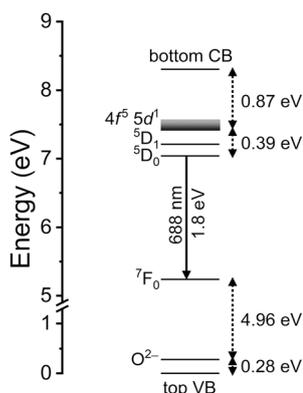
This article contributes to close two gaps in the field of photoexcitable storage nanophosphors because it unveils the photochemical response of a previously unexplored fluorohalide composition and does so using nanocrystals with uniform morphology. Avenues for future work include (i) gaining further synthetic control over nanocrystal average size to probe the size-dependence of photoreduction and dark ionization extents, which impact storage density and stability; and (ii) probing the structural evolution of electron and hole traps during photoreduction and dark ionization to conclusively establish the spatial distribution of these centers and their dynamics.

Conflicts of interest

There are no conflicts to declare.

Data availability

All the data used are provided in the article and the supplementary information (SI). Supplementary information: (1) additional results from X-ray diffraction and electron microscopy analyses, (2) results from thermal analyses, and (3) additional

Fig. 8 Host-referred binding energy diagram of photogenerated Sm^{2+} in BaFBr:Sm^{3+}. The diagram was constructed using a value of 8.3 eV for the bandgap of BaFBr and of 0.87 eV for the $4f^5 5d^1$–CB gap (see text for details).

results from luminescence studies. See DOI: https://doi.org/10.1039/d5tc03810c.

Notes and references

1 K. Takahashi, J. Miyahara and Y. Shibahara, Photostimulated Luminescence (PSL) and Color-Centers in BaFCl-Eu^{2+}, BaFBr-Eu^{2+}, BaFI-Eu^{2+} Phosphors, *J. Electrochem. Soc.*, 1985, **132**, 1492–1494.

2 H. Riesen and W. A. Kaczmarek, Efficient X-ray Generation of Sm^{2+} in Nanocrystalline BaFCl/Sm^{3+}: A Photoluminescent X-ray Storage Phosphor, *Inorg. Chem.*, 2007, **46**, 7235–7237.

3 H. Riesen, K. Badek, T. M. Monro and N. Riesen, Highly Efficient Valence State Switching of Samarium in BaFCl:Sm Nanocrystals in the Deep UV for Multilevel Optical Data Storage, *Opt. Mater. Express*, 2016, **6**, 3097–3108.

4 J. Zhang and H. Riesen, Controlled Generation of Tm^{2+} Ions in Nanocrystalline BaFCl:Tm^{3+} by X-ray Irradiation, *J. Phys. Chem. A*, 2017, **121**, 803–809.

5 J. J. Schuyt and G. V. M. Williams, Radiation-Induced Changes in the Optical Properties of NaMgF$_3$(Sm): Observation of Resettable Sm Radio-Photoluminescence, *Mater. Res. Bull.*, 2018, **106**, 455–458.

6 N. Chowdhury, N. Riesen and H. Riesen, Efficient Generation of Stable Sm^{2+} in Nanocrystalline BaLiF$_3$:Sm^{3+} by UV- and X-Irradiation, *J. Phys. Chem. C*, 2019, **123**, 25477–25481.

7 J. Zhang and H. Riesen, Photostimulated and Persistent Luminescence of Samarium Ions in BaFCl, *J. Lumin.*, 2019, **207**, 188–194.

8 Z. S. Rozaila, N. Riesen and H. Riesen, Luminescence and Photoionization of X-ray Generated Sm^{2+} in Coprecipitated CaF$_2$ Nanocrystals, *Dalton Trans.*, 2021, **50**, 16205–16213.

9 N. Wahib, N. Riesen and H. Riesen, Reversible Mn Valence State Switching in Submicron α-Al$_2$O$_3$:Mn by Soft X-rays and Blue Light – A Potential Pathway Towards Multilevel Optical Data Storage, *Phys. Chem. Chem. Phys.*, 2022, **24**, 6155–6162.

10 J. J. Schuyt, G. V. M. Williams and S. V. Chong, Optically Reversible Tm^{3+} → Tm^{2+} Radiophotoluminescence in NaMgF$_3$:Tm, *Opt. Mater.*, 2022, **133**, 112926.

11 G. Okada, Y. Koguchi, T. Yanagida, S. Kasap and H. Nanto, Recent Advances in Radiophotoluminescence Materials for Luminescence Dosimetry, *Jpn. J. Appl. Phys.*, 2023, **62**, 010609.

12 N. Riesen, X. Pan, K. Badek, Y. Ruan, T. M. Monro, J. Zhao, H. Ebendorff-Heidepriem and H. Riesen, Towards Rewritable Multilevel Optical Data Storage in Single Nanocrystals, *Opt. Express*, 2018, **26**, 12266–12276.

13 N. Riesen, C. Priest, D. G. Lancaster, K. Badek and H. Riesen, Ultra-High-Resolution Greyscale Fluorescence Images via UV-Exposure of Thin Flexible Phosphor Films, *Nanoscale*, 2023, **15**, 4863–4869.

14 M. Matsarski, D. Lovy, H. Bill and K. M. Mohnhaupt, Light-Induced Valence-State Switching in BaFCl:La and SrFCl:La, *Phys. Rev. B: Condens. Matter Mater. Phys.*, 2003, **68**, 205113.

15 R. S. Eachus, W. G. McDugle, R. H. D. Nuttall, M. T. Olm, F. K. Koschnick, T. Hangleiter and J. M. Spaeth, Radiation-Produced Electron and Hole–Centers in Oxygen-Containing BaFBr: 1. EPR and ODEPR Studies, *J. Phys.: Condens. Matter*, 1991, **3**, 9327–9338.

16 R. S. Eachus, W. G. McDugle, R. H. D. Nuttall, M. T. Olm, F. K. Koschnick, T. Hangleiter and J. M. Spaeth, Radiation-Produced Electron and Hole–Centers in Oxygen-Containing BaFBr: 2. An ENDOR Study of O$^-$(F), *J. Phys.: Condens. Matter*, 1991, **3**, 9339–9349.

17 T. J. Bastow, S. N. Stuart, W. G. McDugle, R. S. Eachus and J. M. Spaeth, Oxygen Impurities in X-ray Storage Phosphors BaFBr and BaFCl Investigated by ^{17}O NMR, *J. Phys.: Condens. Matter*, 1994, **6**, 8633–8644.

18 F. K. Koschnick, T. Hangleiter, K. S. Song and J. Spaeth, Optically Detected Magnetic Resonance Study of an Oxygen–Vacancy Complex in BaFBr, *J. Phys.: Condens. Matter*, 1995, **7**, 6925–6937.

19 R. C. Baetzold, Calculation of Properties of Charged Defects in BaFBr and SrFCl, *Phys. Rev. B: Condens. Matter Mater. Phys.*, 1992, **46**, 7994–8002.

20 E. Radzhabov and V. Otroshok, Optical Spectra of Oxygen Defects in BaFCl and BaFBr Crystals, *J. Phys. Chem. Solids*, 1995, **56**, 1–7.

21 R. S. Eachus, R. H. D. Nuttall, M. T. Olm, W. G. McDugle, F. K. Koschnick, T. Hangleiter and J. M. Spaeth, Oxygen Defects in BaFBr and BaFCl, *Phys. Rev. B: Condens. Matter Mater. Phys.*, 1995, **52**, 3941–3950.

22 H. von Seggern, T. Voigt, W. Knüpfer and G. Lange, Physical Model of Photostimulated Luminescence of X-ray Irradiated BaFBr:Eu^{2+}, *J. Appl. Phys.*, 1988, **64**, 1405–1412.

23 F. K. Koschnick, J. M. Spaeth, R. S. Eachus, W. G. McDugle and R. H. D. Nuttall, Experimental Evidence for the Aggregation of Photostimulable Centers in BaFBr:Eu^{2+} Single Crystals by Cross Relaxation Spectroscopy, *Phys. Rev. Lett.*, 1991, **67**, 3571–3574.

24 F. K. Koschnick, J. M. Spaeth and R. S. Eachus, The Influence of Oxide Impurity on the Generation by X-Irradiation of F Centres in BaFBr, *J. Phys.: Condens. Matter*, 1992, **4**, 3015–3029.

25 Z. Q. Liu, M. Stevens-Kalceff and H. Riesen, Photoluminescence and Cathodoluminescence Properties of Nanocrystalline BaFCl:Sm^{3+} X-ray Storage Phosphor, *J. Phys. Chem. C*, 2012, **116**, 8322–8331.

26 M. A. Stevens-Kalceff, Z. Liu and H. Riesen, Cathodoluminescence Microanalysis of Irradiated Microcrystalline and

Nanocrystalline Samarium Doped BaFCl, *Microsc. Microanal.*, 2012, **18**, 1229–1238.

27 N. Riesen, A. François, K. Badek, T. M. Monro and H. Riesen, Photoreduction of Sm^{3+} in Nanocrystalline BaFCl, *J. Phys. Chem. A*, 2015, **119**, 6252–6256.

28 N. Riesen, K. Badek, L. T. Kasim, Y. Ruan, T. M. Monro and H. Riesen, Multilevel Optical Data Storage using Samarium-Doped Matlockite Nanocrystals, *2017 IEEE Photonics Conference (IPC)*, 2017, pp. 599–600.

29 Z. Pan, L. Z. Deng, L. Cheng, Y. H. Yao, D. L. Qi, W. J. Cheng, Z. R. Sun and S. Zhang, Multiphoton Induced Photoreduction in BaFCl:Sm^{3+} Nanocrystals Under Femtosecond Laser Field, *J. Lumin.*, 2023, **263**, 120052.

30 Z. Pan, B. Zheng, L. Deng, Y. Yao, D. Qi, Y. Shen, Z. Sun and S. Zhang, Spectral Phase-Based Valence State Conversion Manipulation in BaFCl:Sm^{3+} Nanocrystals for Multilevel Information Recording and Display, *Opt. Express*, 2024, **32**, 43643–43653.

31 B. Zheng, L. Z. Deng, J. Li, Y. H. Yao, D. L. Qi, Y. C. Shen, Z. R. Sun and S. A. Zhang, Single Femtosecond Laser Pulse-Induced Valence State Conversion in BaFCl:Sm^{3+} Nanocrystals for Low-Threshold Optical Storage, *Nanophotonics*, 2024, **13**, 3709–3715.

32 A. Winnacker, R. M. Shelby and R. M. Macfarlane, Photon-Gated Hole Burning: A New Mechanism Using Two-Step Photoionization, *Opt. Lett.*, 1985, **10**, 350–352.

33 B. D. Dhanapala, H. N. Munasinghe, K. T. Dissanayake, L. Suescun and F. A. Rabuffetti, Expanding the Synthetic Toolbox to Access Pristine and Rare-Earth-Doped BaFBr Nanocrystals, *Dalton Trans.*, 2021, **50**, 16092–16098.

34 D. K. Amarasinghe, K. T. Dissanayake, B. D. Dhanapala and F. A. Rabuffetti, Local Atomic Environment of Yb^{3+} in Alkaline-Earth Fluorohalide Nanocrystals, *CrystEngComm*, 2022, **24**, 5317–5323.

35 K. T. Dissanayake, L. M. Mendoza, P. D. Martin, L. Suescun and F. A. Rabuffetti, Open-Framework Structures of Anhydrous $Sr(CF_3COO)_2$ and $Ba(CF_3COO)_2$, *Inorg. Chem.*, 2016, **55**, 170–176.

36 H. M. Rietveld, Line Profiles of Neutron Powder-Diffraction Peaks for Structure Refinement, *Acta Crystallogr.*, 1967, **22**, 151–152.

37 H. M. Rietveld, A Profile Refinement Method for Nuclear and Magnetic Structures, *J. Appl. Crystallogr.*, 1969, **2**, 65–71.

38 B. H. Toby and R. B. Von Dreele, GSAS-II: The Genesis of a Modern Open-Source All Purpose Crystallography Software Package, *J. Appl. Crystallogr.*, 2013, **46**, 544–549.

39 T. Kurobori, M. Liu and Y. Hirose, Temperature Dependence of the Near-IR Emission and Its Absorption in Oxygen-Doped BaFBr Crystals, *Jpn. J. Appl. Phys.*, 2001, **40**, L642–L645.

40 V. V. Mikhaylin and M. A. Terekhin, Luminescence Excitation in BaF_2-$BaCl_2$ and BaF_2-$BaBr_2$ Synchrotron Radiation, *Rev. Sci. Instrum.*, 1989, **60**, 2545–2547.

41 V. V. Mikhaylin and M. A. Terekhin, Luminescence Excitation of Barium Fluorohalides by Using Synchrotron Radiation, *Nucl. Instrum. Methods Phys. Res., Sect. A*, 1989, **282**, 607–609.

42 Z. Liu, M. A. Stevens-Kalceff and H. Riesen, Effects of Postannealing on the Photoluminescence Properties of Coprecipitated Nanocrystalline BaFCl:Sm^{3+}, *J. Phys. Chem. A*, 2013, **117**, 1930–1934.

43 A. Sillen and Y. Engelborghs, The Correct Use of "Average" Fluorescence Parameters, *Photochem. Photobiol.*, 1998, **67**, 475–486.

44 W. Qin, K. Jang, S. Park, Y.-I. Lee and C. Kim, The Mechanism of Photobleaching in Sm^{2+}-Doped Alkaline-Earth Fluorohalides, *J. Lumin.*, 2005, **113**, 9–16.

45 J. J. Schuyt and G. V. M. Williams, Oxygen-Impurity Charge Transfer in $NaMgF_3$:Ln (Ln = Yb, Sm, or Eu): Establishing the Lanthanide Energy Levels in $NaMgF_3$, *J. Lumin.*, 2019, **211**, 413–417.

46 J. C. Gâcon, J. C. Souillat, J. Seriot, F. Gaume-Mahn and B. Di Bartolo, Some Aspects of the Sm^{2+} Centre Relaxation in BaClF, *J. Lumin.*, 1979, **18–19**, 244–248.

47 R. Jaaniso and H. Bill, f–f and f–d Transition Interference in Sm^{2+}:SrFCl, *Phys. Rev. B: Condens. Matter Mater. Phys.*, 1991, **44**, 2389–2392.

48 Y. R. Shen and W. B. Holzapfel, Effect of Pressure on Energy Levels of Sm^{2+} in BaFCl and SrFCl, *Phys. Rev. B: Condens. Matter Mater. Phys.*, 1995, **51**, 15752–15762.

49 Y. Shen and K. L. Bray, Effect of Pressure and Temperature on 4f–4f Luminescence Properties of Sm^{2+} ions in MFCl crystals (M = Ba, Sr, and Ca), *Phys. Rev. B: Condens. Matter Mater. Phys.*, 1998, **58**, 11944–11958.

50 P. Pal, T. Penhouet, V. D'Anna and H. Hagemann, Effect of Temperature and Pressure on Emission Lifetime of Sm^{2+} Ion Doped in MFX (M = Sr, Ba; X = Br, I) Crystals, *J. Lumin.*, 2013, **142**, 66–74.

51 J. Christmann and H. Hagemann, New Insights Into the Influence of the $4f^5 5d^1$ State in the $4f^6$ Electronic Configuration of Sm^{2+} in Crystal Hosts, *J. Phys. Chem. A*, 2019, **123**, 2881–2887.

52 P. Mikhail, K. Ramseyer, G. Frei, F. Budde and J. Hulliger, Bleaching of Sm^{2+} During Photoluminescence and Cathodoluminescence, *Opt. Commun.*, 2001, **188**, 111–117.

53 J. J. Schuyt and G. V. M. Williams, Quenching of the Sm^{2+} Luminescence in $NaMgF_3$:Sm via Photothermal Ionization: Alternative Method to Determine Divalent Lanthanide Trap Depths, *Appl. Phys. Lett.*, 2019, **115**, 181104.

54 Z.-y He, Y.-s Wang, S. Li and X.-r Xu, Dynamic Studies on the Time-Resolved Fluorescence of Sm^{2+} in $BaCl_2$, *J. Lumin.*, 2002, **97**, 102–106.

55 J. F. Scott, Raman Spectra of BaClF, BaBrF, and SrClF, *J. Chem. Phys.*, 1968, **49**, 2766–2769.

56 L. Cui, Z. Dong, D. Yu, Y. Wang and A. Meijerink, High-Sensitivity Luminescent Temperature Sensors: MFX:1%Sm^{2+} (M = Sr, Ba, X = Cl, Br), *Sci. Adv.*, 2024, **10**, eado7737.

57 K. Takahashi, K. Kohda, J. Miyahara, Y. Kanemitsu, K. Amitani and S. Shionoya, Mechanism of Photostimulated Luminescence in BaFX:Eu^{2+} (X = Cl,Br) Phosphors, *J. Lumin.*, 1984, **31–32**, 266–268.

58 T. Inerbaev, A. Akilbekov, D. Kenbayev, A. Dauletbekova, A. Shalaev, E. Polisadova, M. Konuhova, S. Piskunov and A. I. Popov, Color Centers in BaBr Crystals: Experimental Study and Theoretical Modeling, *Materials*, 2024, **17**, 3340.